

# Catalysis Science & Technology

Accepted Manuscript



This is an *Accepted Manuscript*, which has been through the Royal Society of Chemistry peer review process and has been accepted for publication.

*Accepted Manuscripts* are published online shortly after acceptance, before technical editing, formatting and proof reading. Using this free service, authors can make their results available to the community, in citable form, before we publish the edited article. We will replace this *Accepted Manuscript* with the edited and formatted *Advance Article* as soon as it is available.

You can find more information about *Accepted Manuscripts* in the [Information for Authors](#).

Please note that technical editing may introduce minor changes to the text and/or graphics, which may alter content. The journal's standard [Terms & Conditions](#) and the [Ethical guidelines](#) still apply. In no event shall the Royal Society of Chemistry be held responsible for any errors or omissions in this *Accepted Manuscript* or any consequences arising from the use of any information it contains.

## ARTICLE

# Catalytic Oxidation of Formaldehyde over Manganese Oxides with Different Crystal Structure

Cite this: DOI: 10.1039/x0xx00000x

Jianghao Zhang, Yaobin Li, Lian Wang, Changbin Zhang\*, Hong He

Received 00th January 2012,  
Accepted 00th January 2012

DOI: 10.1039/x0xx00000x

[www.rsc.org/](http://www.rsc.org/)

The  $\alpha$ -,  $\beta$ -,  $\gamma$ - and  $\delta$ -MnO<sub>2</sub> catalysts were prepared by hydrothermal method and tested for the catalytic oxidation of formaldehyde (HCHO) at low temperature. The dramatic differences in activities among the MnO<sub>2</sub> with different crystal structure were observed.  $\delta$ -MnO<sub>2</sub> catalyst exhibited the best activity among four catalysts and achieved the nearly complete HCHO conversion at 80°C, while  $\alpha$ -,  $\beta$ - and  $\gamma$ -type MnO<sub>2</sub> obtained the 100% HCHO conversion at 125°C, 200°C, 150°C, respectively. The catalysts were next characterized by Brunauer-Emmett-Teller (BET), X-ray diffraction (XRD), Field-Emission Scanning Electron Microscope (FE-SEM), Temperature-programmed reduction by H<sub>2</sub> (H<sub>2</sub>-TPR), X-ray photoelectron spectroscopy (XPS) and Temperature-programmed desorption of HCHO (HCHO-TPD) methods to investigate the factors influencing the catalytic activity. Based on the characterization results, it is supposed that the tunnel structure and active lattice oxygen species are the main factors that contribute to the excellent performance of  $\delta$ -MnO<sub>2</sub>. According to the high catalytic performance and facile preparation process, the  $\delta$ -MnO<sub>2</sub> may potentially be used as a support in applications of supported catalysts.

## 1. Introduction

Formaldehyde (HCHO) emitted from widely used building and decorative materials has become the main indoor air pollutant in airtight houses.<sup>1</sup> Exposure to HCHO may cause several of the syndromes: eye, nose or throat irritation; coughing; fatigue and severe allergic reactions, etc.<sup>2,3</sup> According to the latest study, HCHO is also harmful to the nervous system and cardiovascular system.<sup>4</sup> Hence, effective abatement of indoor air HCHO is urgently needed in order to elevate the living air condition and reduce the public health risk.

Several approaches for HCHO removal have been studied during decades' research, including photo-catalytic oxidation,<sup>5,6</sup> plasma decomposition with catalyst,<sup>7</sup> adsorption<sup>8</sup> and catalytic oxidation.<sup>9-11</sup> However, photo-catalytic oxidation need light containing ultraviolet to excite the catalyst, and may lead to the formation of harmful by-products. Plasma technology has significant limitations such as the poor performance under low concentrations of HCHO and possible harmful by-product such as ozone.<sup>2</sup> The effectiveness of adsorption materials is limited by the maximum capacity and the hazard of desorption during regeneration. Catalytic oxidation method spurns the above drawbacks and could selectively decompose low concentration toxic HCHO to harmless CO<sub>2</sub> and H<sub>2</sub>O even at ambient temperature. It has shown to be a promising method for indoor air HCHO removal.<sup>12</sup>

There are two main kinds of catalysts for HCHO oxidation including supported noble metal (Pt, Au, Rh and Pd)<sup>13-18</sup> and none-

noble metal oxides (Ag, Co, Ce and Mn)<sup>10, 19-24</sup> catalysts. The supported noble metal catalysts such as alkali-metal-doped Na-Pt/TiO<sub>2</sub>,<sup>9, 25</sup> Pt/MnO<sub>x</sub>-CeO<sub>2</sub>,<sup>16</sup> TiO<sub>2</sub> supported Pd nanoparticles,<sup>17</sup> Na-promoted Pd/TiO<sub>2</sub>,<sup>18</sup> have shown the remarkable catalytic activities at ambient temperature even at high space velocity. However, the high price inhibited their wide application. In contrast, the transitional-metal oxides are much cheaper; some catalysts have also demonstrated to be effective for low temperature HCHO oxidation. Therefore, the transitional metal oxide is regarded as a promising alternative catalyst to noble metal catalyst.

Mn based catalysts are widely studied for HCHO oxidation and appeared to be the most active catalyst among the transitional-metal oxides. It was reported that the preparation method, morphology, tunnel structures, etc, have the considerable influence on the catalytic activity of Mn based catalysts. Tang et al. reported that MnO<sub>x</sub>-CeO<sub>2</sub> prepared by modified co-precipitation method showed the better performance than those prepared with sol-gel or co-precipitation methods, achieving the complete HCHO conversion at 373 K.<sup>26</sup> Chen et al. found that the MnO<sub>x</sub> with hollow nanostructure had a much higher activity than that with honeycomb nanostructure.<sup>27</sup> Chen et al. studied the tunnel structure effect on Mn oxides activity and suggested that the [2×2] tunnel structure could dramatically elevate the catalytic activity of Mn oxides.<sup>28</sup> Wang et al. observed that the 3D ordered cubic mesoporous Co-Mn oxide is highly effective catalyst for HCHO oxidation and obtained the complete oxidation of HCHO at 70 °C.<sup>29</sup>

In this study, the MnO<sub>2</sub> with  $\alpha$ -,  $\beta$ -,  $\gamma$ - and  $\delta$ -phase structures were prepared by hydrothermal process and then tested their performance for the catalytic oxidation of formaldehyde (HCHO) at low temperature. The dramatic difference about the catalytic activity was clearly observed on the four kinds of MnO<sub>2</sub>. The  $\delta$ -MnO<sub>2</sub> showed the best catalytic activity of the four kinds, achieving almost 100% conversion of 170 ppm HCHO at 80 °C with a gas hourly space velocity of 100 000 mL (g<sub>cat</sub>·h)<sup>-1</sup>. The catalysts were carefully characterized by XRD, BET, FE-SEM, H<sub>2</sub>-TPR, XPS and HCHO-TPD measurements. Based on the results, the factors affecting the catalytic activity were elucidated.

## 2. Experimental section

### 2.1 Preparation of Catalysts

The four kinds of manganese oxides with different phase structures were prepared by hydrothermal method according to the previous report.<sup>30</sup> For the  $\alpha$ -MnO<sub>2</sub>, 0.525g MnSO<sub>4</sub>·H<sub>2</sub>O and 1.25g KMnO<sub>4</sub> were mixed in 80 mL distilled water, then it was stirred magnetically about 30 min to form homogeneous solution before it was moved into a Teflon-lined stainless steel autoclave (100 mL). After that, the autoclave was heated to 160 °C for 12h in an oven. The product was collected, washed, filtered, dried at 80 °C and then calcined at 300 °C. The procedures of preparation of other manganese oxides were similar to  $\alpha$ -MnO<sub>2</sub> except for the precursor, the reaction temperature and the duration.

For  $\beta$ -MnO<sub>2</sub>, 1.69g MnSO<sub>4</sub>·H<sub>2</sub>O and 2.28g (NH<sub>4</sub>)<sub>2</sub>S<sub>2</sub>O<sub>8</sub> reacted at 140 °C for 12h.

For  $\gamma$ -MnO<sub>2</sub>, 3.375g MnSO<sub>4</sub>·H<sub>2</sub>O and 4.575g (NH<sub>4</sub>)<sub>2</sub>S<sub>2</sub>O<sub>8</sub> reacted at 90 °C for 24h.

For  $\delta$ -MnO<sub>2</sub>, 0.275g MnSO<sub>4</sub>·H<sub>2</sub>O and 1.5g KMnO<sub>4</sub> were heated to 240 °C for 24h.

### 2.2 Characterization

The structure parameter, pore characterization and specific surface area of the samples were obtained by the BET plot using a Quantachrome Quadrasorb SI-MP at -196 °C over the whole range of relative pressures. The pore size distribution was calculated by the desorption branch of the N<sub>2</sub> adsorption isotherm using the BJH method. Before the N<sub>2</sub> physisorption, the catalysts were degassed at 300 °C for 5h.

XRD patterns were measured on an X'Pert PRO MPD X-ray powder diffractometer with a Cu K $\alpha$  radiation operated at 40 kV and 40 mA. The 2 $\theta$  angle ranged from 10° to 80° with a scan step of 0.02°.

Field-Emission Scanning Electron Microscope (FE-SEM) images were obtained by SU-8020 scanning electron microscope. The samples for FE-SEM measurements were prepared by the powder depositing on a conductive tape using N<sub>2</sub> vertical purging. The voltage exerted for lower amplifying was 3kV while for higher amplifying was 1kV.

Temperature-programmed reduction (TPR) were carried out on Chemisorption Analyzer (AutoChem 2920) equipped with a TCD detector. After sweeping by Ar and air successively, a flow of 10% H<sub>2</sub>/Ar at a rate of 50 cm<sup>3</sup> min<sup>-1</sup> (STP) passed the samples with the temperature increasing from 100 to 600 °C at a rate of 10 °C min<sup>-1</sup>.

The H<sub>2</sub> consumption was monitored by TCD after produced H<sub>2</sub>O removal.

X-ray photoelectron spectroscopy (XPS) profile was obtained by an AXIS Ultra system, equipped with an Al K $\alpha$  radiation ( $h\nu=1486.6$  eV) with anode operated at 225 W and 15 kV. The binding energy values were calibrated by C 1s peak (284.8 eV). The surface relative composition was estimated from the integrated intensities corrected by atomic sensitive factors.

The temperature-programmed desorption of HCHO (HCHO-TPD) measurements on the samples were carried out on a Micromeritics AutoChem II 2920 instrument. The catalysts were loaded in a quartz reactor and heated at 200 °C for 0.5 h in the Argon flow to remove the absorbed CO<sub>2</sub> and H<sub>2</sub>O. After being cooled down to -20 °C, the samples were saturated by HCHO/Helium mixture gas for 1 h. Then the flow gas was changed to pure helium for 0.5 h, followed by the temperature ramping to 250 °C at a linear rate of 10 °C min<sup>-1</sup>. The product of HCHO and CO<sub>2</sub> were monitored by Cirrus II Mass Spectrometer at the m/e ratios of 30 and 44, respectively.

### 2.3 Activity Test

The activity tests for the catalytic oxidation of HCHO over the catalysts (60 mg) were performed in a fixed-bed quartz flow reactor (i.d. = 4 mm) in an incubator. Gaseous HCHO was generated by flowing nitrogen through the paraformaldehyde container in a water bath kept at 35 °C. The feed gas composition is 170 ppm HCHO, 20% O<sub>2</sub> and 25% RH balanced by N<sub>2</sub>. The total flow rate was 100 mL min<sup>-1</sup>, corresponding to a gas hourly space velocity (GHSV) of 100 000 mL (g<sub>cat</sub>·h)<sup>-1</sup>. The  $\delta$ -MnO<sub>2</sub> was also tested under a high GHSV of 600, 000 mL (g<sub>cat</sub>·h)<sup>-1</sup> to control HCHO conversion below 100% for the measurement of specific reaction rate.

As the same with our previous activity evaluating instrument and method,<sup>9, 18</sup> the inlet and outlet gases were monitored by FTIR (Nicolet iS50) equipped with 2 m gas cell and a DTGS detector; resolution: 0.5 cm<sup>-1</sup>; OPD velocity: 0.4747 cm s<sup>-1</sup>. The collect region was 4000-600 cm<sup>-1</sup> and the number of scans per spectrum was 16 times. HCHO and CO<sub>2</sub> was measured by the peaks located at 2897 (C-H vibration) and 2350 cm<sup>-1</sup> (O-C-O vibration), respectively. Since no other carbon containing compounds except for CO<sub>2</sub> were detected in the effluents for all tested catalysts, the HCHO and CO<sub>2</sub> concentrations were quantified and calculated based on the peak area of CO<sub>2</sub> at 2350 cm<sup>-1</sup>.

The lattice oxygen test experiments were also carried out over  $\delta$ -MnO<sub>2</sub> to check the role of lattice oxygen species in HCHO oxidation reaction. The initial HCHO concentration, catalyst amount and GHSV were the same as the normal activity test experiment. In detail of the procedure, the samples were first pretreated at 150 °C for 30 min in flow of pure O<sub>2</sub> of 20 mL min<sup>-1</sup>. Then the purging gas was switched to pure N<sub>2</sub> of 100 mL min<sup>-1</sup> for 30 min to remove gaseous O<sub>2</sub> and the weak absorbed oxygen species. After that, the temperatures was lowered to X °C (X=50, 75) and then the HCHO balanced with N<sub>2</sub> was introduced into reactor and the products were monitored by FTIR.

## 3. Results and discussion

### 3.1 Crystal structure and morphology of catalyst

XRD patterns were measured to investigate the crystallographic structures of the samples and the results are shown in Fig. 1. All of

the four samples could be well indexed and in good agreement with the lattice constants of  $\alpha$ -MnO<sub>2</sub> (JCPDS 44-0141),  $\beta$ -MnO<sub>2</sub> (JCPDS 24-0735),  $\gamma$ -MnO<sub>2</sub> (JCPDS 14-0644) and  $\delta$ -MnO<sub>2</sub> (JCPDS 80-1098), respectively, confirming the successful preparation of MnO<sub>2</sub> with four types of crystal structures, which were also verified by the Raman spectra and lattice distances measured by high-resolution transmission electron microscope (HR-TEM) (supplementary information, Fig. S1 and Fig. S2). In addition, it could be inferred that  $\alpha$ -MnO<sub>2</sub> and  $\beta$ -MnO<sub>2</sub> had high crystallinity according to their narrow peaks width and high intensities. In contrast,  $\gamma$ -MnO<sub>2</sub> presented a very poor XRD patterns. As reported,  $\gamma$ -MnO<sub>2</sub> is normally the product of irregular intergrowth of elements of ramsdellite and pyrolusite,<sup>31, 32</sup> thus no complete single crystal will emerge in structure, leading to low crystallinity of  $\gamma$ -MnO<sub>2</sub>.  $\delta$ -MnO<sub>2</sub> generally has the disordered structures in certain crystallographic directions.<sup>33</sup> Therefore,  $\delta$ -MnO<sub>2</sub> showed a much broader and weaker XRD peaks than those of the  $\alpha$ -MnO<sub>2</sub> and  $\beta$ -MnO<sub>2</sub>.

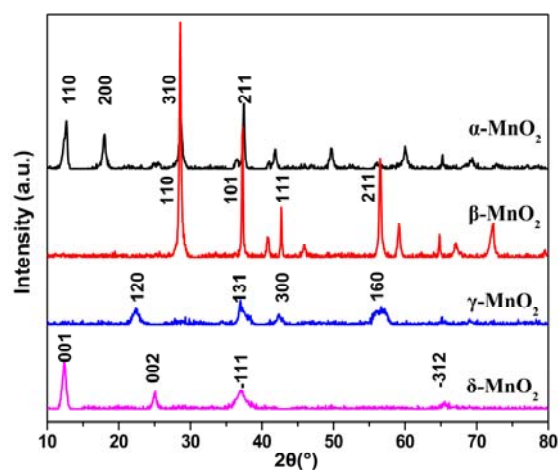


Fig. 1 XRD patterns of  $\alpha$ -,  $\beta$ -,  $\gamma$ - and  $\delta$ -MnO<sub>2</sub> samples.

Table 1 shows the specific surface areas ( $S_{\text{BET}}$ ), average pore sizes ( $d$ ), and total pore volumes ( $V$ ) of four samples. The  $\delta$ -MnO<sub>2</sub> showed the highest  $S_{\text{BET}}$ , average pore size ( $d$ ) and  $V$  among four catalysts. The  $\alpha$ - and  $\gamma$ -MnO<sub>2</sub> exhibited much similar moderate values of  $S_{\text{BET}}$ ,  $d$  and  $V$ . In contrast,  $\beta$ -MnO<sub>2</sub> presented the lowest parameters.

**Table 1** Specific surface area (BET), average pore size ( $d$ ), total pore volume ( $V$ ) and normalized reaction rate ( $R_s$ ) of  $\alpha$ -,  $\beta$ -,  $\gamma$ - and  $\delta$ -MnO<sub>2</sub> catalysts.

samples	$S_{\text{BET}}$ [m <sup>2</sup> g <sup>-1</sup> ]	Pore diameter [nm]	Pore volume [cm <sup>3</sup> g <sup>-1</sup> ]	$R_s$ [nmol s <sup>-1</sup> m <sup>-2</sup> ]
$\alpha$ -MnO <sub>2</sub>	80.8	13.2	0.27	1.87
$\beta$ -MnO <sub>2</sub>	23.3	11.4	0.05	0.63
$\gamma$ -MnO <sub>2</sub>	85.3	12.2	0.26	0.44
$\delta$ -MnO <sub>2</sub>	108.4	14.1	0.38	9.42

FE-SEM images of  $\alpha$ -,  $\beta$ -,  $\gamma$ - and  $\delta$ -MnO<sub>2</sub> samples (two magnifications for each) are shown in Fig. 2. The  $\alpha$ -MnO<sub>2</sub> showed a dendritic nanostructure (Fig. 2a) which was composed of uniform nanorods; the length of each individual nanorod is about 2.5  $\mu\text{m}$  long and 30 nm width. The  $\beta$ -MnO<sub>2</sub> had similar dendritic nanostructures (Fig. 2b) which consisted of tetragonal prism nanorods with 2  $\mu\text{m}$  long and 50-100 nm width. The  $\gamma$ -MnO<sub>2</sub> displayed a spherical

nanostructure which was composed of MnO<sub>2</sub> nanoneedles with sharp tips. The  $\gamma$ -MnO<sub>2</sub> nanoneedles had the lengths of about 2.5  $\mu\text{m}$  and diameters of about 40 nm. The  $\delta$ -MnO<sub>2</sub> also has a spherical morphology with 2-3  $\mu\text{m}$  diameter, which was built up of many interleaving nanoflakes composed of the very thin nanowire with 10-20 nm width. The morphology of the samples were also surveyed by HRTEM (supplementary information, Fig. S2), which showed consistent results with the SEM images.

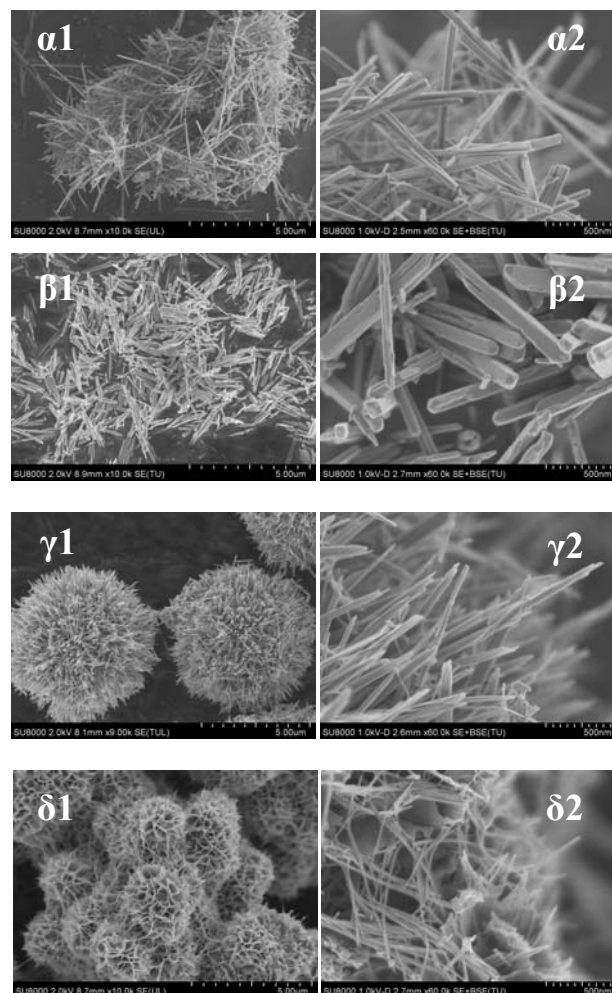


Fig. 2 SEM images of  $\alpha$ -,  $\beta$ -,  $\gamma$ - and  $\delta$ -MnO<sub>2</sub> samples, 1 and 2 refer to different magnifications of one sample.

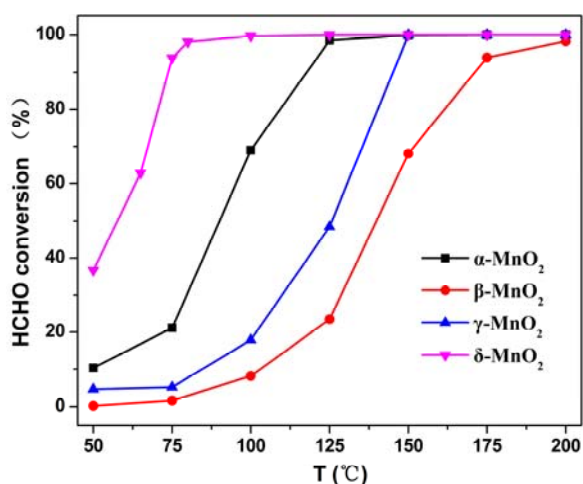
### 3.2 Activity Test

Fig. 3 shows the HCHO conversion to CO<sub>2</sub> as a function of temperature over the  $\alpha$ -,  $\beta$ -,  $\gamma$ - and  $\delta$ -MnO<sub>2</sub> catalysts at a GHSV of 100,000 mL (g<sub>cat</sub> · h)<sup>-1</sup> with the inlet HCHO concentration of 170 ppm. The temperature dependence of HCHO conversions were distinctly related to the phase structures of MnO<sub>2</sub>. The catalytic activities followed the sequence of  $\delta$ -> $\alpha$ -> $\gamma$ -> $\beta$ -MnO<sub>2</sub>. The  $\delta$ -MnO<sub>2</sub> showed the best catalytic activity among the four samples and the 100% HCHO conversion was obtained at around 80 °C. While other catalysts  $\alpha$ -,  $\beta$ - and  $\gamma$ -MnO<sub>2</sub> exhibited the much lower activity than the  $\delta$ -MnO<sub>2</sub> with 100% HCHO conversions achieved at 125 °C, 200 °C, 150 °C, respectively. The above findings clearly showed that the catalytic activity of MnO<sub>2</sub> for oxidation of HCHO was in tight correlation with the crystal structures. In order to eliminate the



influence of surface area, specific reaction rate ( $R_s$ ) at 100 °C in term of generated amount of  $\text{CO}_2$  per unit area is calculated and given in Table 1. For  $R_s$  measurement, the  $\delta\text{-MnO}_2$  was tested under a high GHSV of  $600,000 \text{ mL (g}_{\text{cat}} \cdot \text{h)}^{-1}$  with the conversion of 80.5% at 100 °C. As shown in Table 1,  $R_s$  of  $\delta\text{-MnO}_2$  is  $9.42 \text{ nmol s}^{-1} \text{ m}^{-2}$ , which is much higher (around 5 times of the second best) than other catalysts. These results indicate that the oxidation of HCHO is drastically enhanced on the  $\delta\text{-MnO}_2$  catalysts, implying the  $\delta\text{-MnO}_2$  could be the potential catalyst for HCHO oxidation. Liang et al.<sup>30</sup> have tested the catalytic properties of  $\alpha$ -,  $\beta$ -,  $\gamma$ - and  $\delta\text{-MnO}_2$  catalysts for CO oxidation. They observed that the catalytic activities decreased in the order of  $\alpha \approx \delta > \gamma > \beta\text{-MnO}_2$  and the  $\alpha\text{-MnO}_2$  has a similar activity to  $\delta\text{-MnO}_2$ . However, in the study, the series of catalysts showed a different catalytic behaviour for HCHO oxidation and the  $\delta\text{-MnO}_2$  is much more active than  $\alpha\text{-MnO}_2$ . Therefore, the key factor affecting the activity of  $\text{MnO}_2$  catalyst should be different for these two reactions.

The stability of  $\delta\text{-MnO}_2$  catalyst was checked by long isothermal tests at 75 °C with a GHSV of  $150,000 \text{ mL (g}_{\text{cat}} \cdot \text{h)}^{-1}$ . As shown in Fig. 4, in the beginning, there is a certain rise of the conversion rate which might due to some highly active and non-renewable adsorbed oxygen species. And then the rate dropped and stabilized at around 60%. Overall, the sample exhibited the excellent stability and efficiency, and the approximately 60 % HCHO conversion rate was maintained over a 30 h-long test. After reaction and stability test, the XRD patterns of four catalysts have been also measured, and the results showed that their crystalline structures remained intact (supplementary information, Fig. S3).



**Fig. 3** HCHO conversions over  $\alpha$ -,  $\beta$ -,  $\gamma$ - and  $\delta\text{-MnO}_2$  samples. Reaction conditions: 170 ppm of HCHO, 20%  $\text{O}_2$ ,  $\text{N}_2$  balance, GHSV= $100\,000 \text{ mL (g}_{\text{cat}} \cdot \text{h)}^{-1}$ .

**Table 2** The  $\text{K}^+$  content determined by ICP-OES and the XPS data for  $\alpha$ -,  $\beta$ -,  $\gamma$ - and  $\delta\text{-MnO}_2$  samples.

samples	$\text{K}^+$ content [wt%]	Binding energy [eV]		molecular ratio $\text{Mn}^{4+}/\text{Mn}^{3+}$	Binding energy [eV]		molecular ratio $\text{O}_{\text{latt}}/\text{O}_{\text{ads}}$
		$\text{Mn}^{4+}$	$\text{Mn}^{3+}$		$\text{O}_{\text{latt}}$	$\text{O}_{\text{ads}}$	
$\alpha\text{-MnO}_2$	7.1	642.6	641.8	5.6	529.7	531.3	4.1
$\beta\text{-MnO}_2$	0	642.2	641.5	4.2	529.3	530.8	2.4
$\gamma\text{-MnO}_2$	0	642.6	641.8	4.0	529.7	531.3	2.8
$\delta\text{-MnO}_2$	6.4	642.5	641.8	8.3	529.6	531.3	5.5

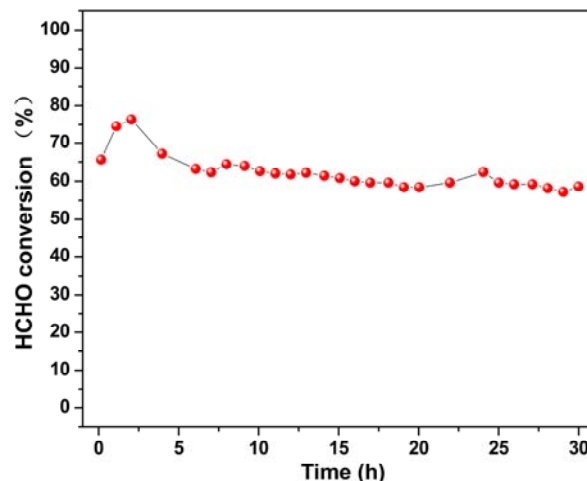


**Fig. 4** Stability test of  $\delta\text{-MnO}_2$  catalyst in terms of the production amount of  $\text{CO}_2$ . Reaction conditions: 75 °C, 170 ppm of HCHO, 20%  $\text{O}_2$ ,  $\text{N}_2$  balance, GHSV= $150\,000 \text{ mL (g}_{\text{cat}} \cdot \text{h)}^{-1}$ .

### 3.3 Effect of $\text{K}^+$

There are several factors that might influence the activity of manganese oxides. Hou et al.<sup>34</sup> have reported that increasing  $\text{K}^+$  content would drastically enhance the catalytic activity of OMS-2 catalysts for catalytic oxidation of benzene. Therefore, we first investigated the possible effect of  $\text{K}^+$  species on the catalytic activity of the series of  $\text{MnO}_2$  for HCHO oxidation. ICP-OES was carried out to measure the  $\text{K}^+$  contents in the four catalysts and the quantitative results were summarized in Table 2. The  $\text{K}^+$  volume in  $\alpha\text{-MnO}_2$  and  $\delta\text{-MnO}_2$  was 7.1 wt. % and 6.4 wt. %, respectively, and no  $\text{K}^+$  was detected in  $\beta$ - and  $\gamma\text{-MnO}_2$  catalysts. The amount of  $\text{K}^+$  in  $\alpha\text{-MnO}_2$  (7.1 wt. %) was slightly higher than that in  $\delta\text{-MnO}_2$  (6.4 wt. %), however, the  $\alpha\text{-MnO}_2$  showed a much lower activity for HCHO oxidation than  $\delta\text{-MnO}_2$ , indicating that  $\text{K}^+$  presence was not the reason for the activity difference between these two catalysts. The  $\alpha\text{-MnO}_2$  without  $\text{K}^+$  species was next prepared following the procedures reported by Hou et al.<sup>34</sup> and then tested in the same condition as the normal activity test. The activity comparison of the two kinds of  $\alpha\text{-MnO}_2$  samples as well as the  $\gamma\text{-MnO}_2$  is shown in Fig. 5. It is indicated that the activity of  $\alpha\text{-MnO}_2$  slightly dropped in the absence of  $\text{K}^+$  species, but is still much higher than  $\gamma\text{-MnO}_2$ . Thus, it could be concluded that the  $\text{K}^+$  species was not the main factor of affecting activities of four types of  $\text{MnO}_2$  catalysts for the HCHO oxidation.

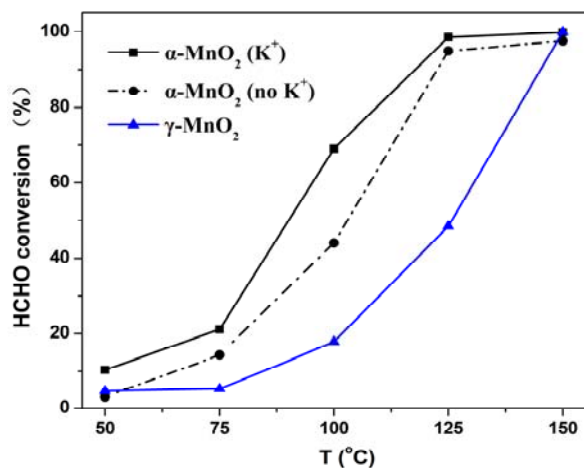


Fig. 5 Activity test of the three samples of  $\alpha$ - with/without K<sup>+</sup> and  $\gamma$ -MnO<sub>2</sub>. Reaction conditions: 170 ppm of HCHO, 20% O<sub>2</sub>, N<sub>2</sub> balance, GHSV=100 000 mL (g<sub>cat</sub>·h)<sup>-1</sup>.

### 3.4 Tunnel Structure

As reported, the four kinds of MnO<sub>2</sub> catalysts contain the different types of tunnel structures.<sup>35</sup> The  $\alpha$ -MnO<sub>2</sub> consists of [2×2] and [1×1] tunnel structures. The  $\beta$ -MnO<sub>2</sub> is composed of [1×1] tunnel structure. The  $\gamma$ -MnO<sub>2</sub> contains of both [1×1] and [1×2] tunnels. In contrast, the  $\delta$ -MnO<sub>2</sub> forms a 2D layer structure. Therefore, the distinction in activities of MnO<sub>2</sub> might be partially ascribed from the different tunnel structures. Liang et al.<sup>30</sup> have reported that the tunnel structure could affect the CO chemisorption, therefore obviously influencing the catalytic activity of MnO<sub>2</sub> for CO oxidation. In addition, Chen et al.<sup>28</sup> have observed that MnO<sub>2</sub> with the [2×2] tunnel structure is much more active than MnO<sub>2</sub> with the [1×1] or [3×3] structure for HCHO oxidation since that the effective diameter of [2×2] tunnel is more suitable for the HCHO diffusion during the reaction. Our results were consistent with the reported result in that  $\alpha$ - was more active than  $\beta$ - and  $\gamma$ -. Moreover, the present results also suggested that the interlayer structure of MnO<sub>2</sub> would more benefit for the HCHO oxidation reaction than [2×2] tunnel structure by facilitating the absorption and diffusion of HCHO molecules to active sites. Therefore, the different tunnel structure among  $\alpha$ -,  $\beta$ -,  $\gamma$ - and  $\delta$ -MnO<sub>2</sub> catalysts should be one of the reasons for their different activities.

### 3.5 Reducibility of Catalyst

H<sub>2</sub>-TPR experiments were next performed to investigate the reducibility of the four samples. Fig. 6 shows the H<sub>2</sub>-TPR profiles of the  $\alpha$ -,  $\beta$ -,  $\gamma$ - and  $\delta$ -MnO<sub>2</sub> catalysts. The  $\beta$ -MnO<sub>2</sub> presented a sharp peak at 301 °C with a broad peak at 419 °C, respectively. Accounting for the peak area which could indicate the hydrogen consumption amount, the ratio of lower temperature peak to the higher one is about 2:1. This is the typical feature of the reduction of MnO<sub>2</sub> with the process of MnO<sub>2</sub> to Mn<sub>3</sub>O<sub>4</sub>, which lead to the lower temperature peak, and then Mn<sub>3</sub>O<sub>4</sub> to MnO leading to the higher temperature one.<sup>34</sup> The pattern of  $\gamma$ -MnO<sub>2</sub> with the location of peaks at 305 °C and 403 °C exhibited certain similarity with  $\beta$ -MnO<sub>2</sub>, and that shows the same reduction procedures as the  $\beta$ -MnO<sub>2</sub>. In contrast, the  $\alpha$ -MnO<sub>2</sub> exhibited two reduction peaks at 292 °C and 319 °C, respectively. Similarly, the  $\delta$ -MnO<sub>2</sub> also showed two overlapped

reduction peaks located at 269 °C and 285 °C. However, the ratio of the lower temperature peak to the higher temperature peak was about 1:1, which may indicate the existence of a different reduction route, that is MnO<sub>2</sub> to Mn<sub>2</sub>O<sub>3</sub> and then to MnO. Nevertheless, it is clear from these results that the reduction capacity sequence should be  $\delta$ -> $\alpha$ -> $\gamma$ - $\approx$  $\beta$ -, which is consistent with the previous report.<sup>30</sup> The reducibility tested by H<sub>2</sub>-TPR could reflect the oxygen mobility in the samples, since the  $\delta$ -MnO<sub>2</sub> shows the reduction peak at the lowest temperature, it was proved to possess the most mobile oxygen species both in surface and bulk among the four catalysts. Consequently, the high oxygen mobility cause more oxygen to be adsorbed and further excited to active oxygen, which would then be involved in the reaction.

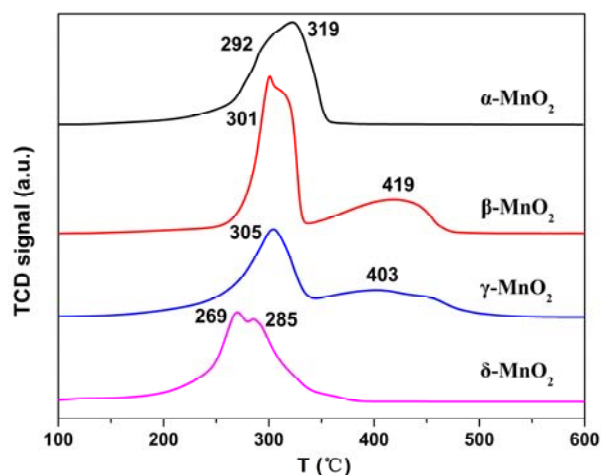


Fig. 6 H<sub>2</sub>-TPR profiles of  $\alpha$ -,  $\beta$ -,  $\gamma$ - and  $\delta$ -MnO<sub>2</sub> samples.

### 3.6 XPS Analysis

To identify the states of surface Mn and O elements and check our deduction from the H<sub>2</sub>-TPR experiment, XPS spectra were next measured. Fig. 7a shows the Mn2p<sub>3/2</sub> spectra of the series of catalysts. The peaks at 642.6 and 641.8 eV could be attributed to the surface Mn<sup>4+</sup> and Mn<sup>3+</sup>, respectively.<sup>36-37</sup> The Mn2p<sub>3/2</sub> peak of  $\beta$ -MnO<sub>2</sub> exhibited a certain shift of about 0.4 eV to low binding energy, (supplementary information, Fig. S4). This shift could be regarded as a system shift because it also emerged at the O 1s peak (Fig. 7b). Thus, after the spectra were deconvoluted, the peaks of both Mn<sup>4+</sup> and Mn<sup>3+</sup> in  $\beta$ -MnO<sub>2</sub> shifted to lower binding energy with about 0.4 eV. A quantitative analysis on Mn2p<sub>3/2</sub> spectra was performed and the surface element molar ratios of Mn<sup>4+</sup>/Mn<sup>3+</sup> are summarized in Table 2. Apparently, the surface Mn<sup>4+</sup>/Mn<sup>3+</sup> molar ratios of the catalysts were distinct in MnO<sub>2</sub> with different crystal structures. The  $\delta$ -MnO<sub>2</sub> sample presented the highest Mn<sup>4+</sup>/Mn<sup>3+</sup> molar ratio (8.3). The sequence of surface Mn<sup>4+</sup> percentage followed the order of  $\delta$ -> $\alpha$ -> $\gamma$ - $\approx$  $\beta$ -.

The XPS spectra of O1s are shown in Fig. 7b. The asymmetrical O1s spectra could be deconvoluted to two peaks. The main species at binding energy 529.7 eV was assigned to the lattice oxygen (O<sup>2-</sup>) (denoted as O<sub>latt</sub>),<sup>37, 38, 39</sup> and the binding energy of 531.3 corresponded to the surface adsorbed oxygen with low coordination (denoted as O<sub>ads</sub>)<sup>37, 40</sup> such as O<sub>2</sub><sup>2-</sup> or O<sup>-</sup> belonging to

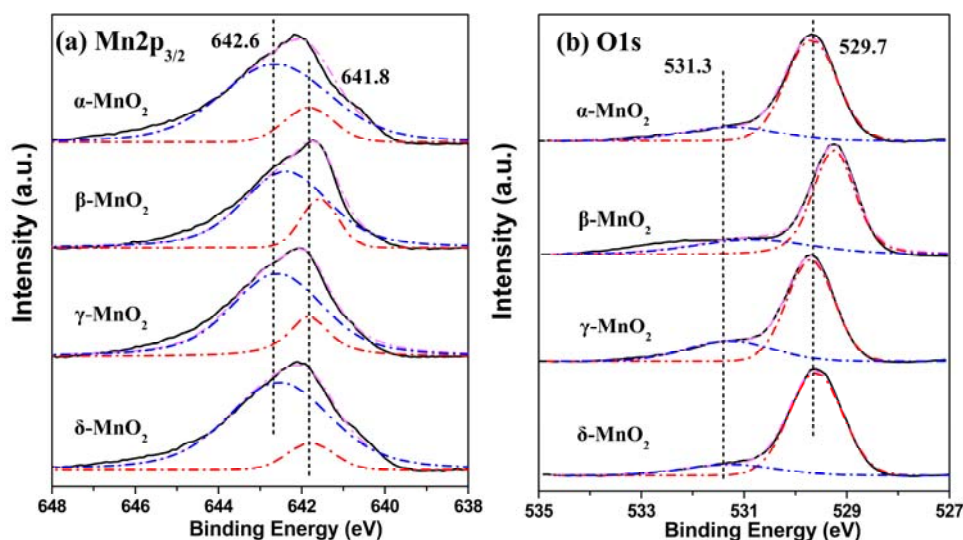


Fig. 7 XPS spectra of  $\alpha$ -,  $\beta$ -,  $\gamma$ - and  $\delta$ -MnO<sub>2</sub> samples: (a) Mn2p<sub>3/2</sub> and (b) O1s.

defect-oxide or hydroxyl-like group. Different from other samples, the O 1s peaks of  $\beta$ -MnO<sub>2</sub> shifted towards lower binding energy with about 0.4 eV, consisting with previous studies<sup>30, 41, 42</sup> and the results of Mn 2p spectra. In view of the system shift with 0.4 eV on the spectra of  $\beta$ -MnO<sub>2</sub>, the binding energy locations of both O<sub>ads</sub> and O<sub>latt</sub> in the  $\beta$ - are also pitched with a shift about 0.4 eV when the deconvolution is carried out. The surface element molar ratio of O<sub>latt</sub>/O<sub>ads</sub> were calculated and summarized in Table 2. They followed the sequence of  $\delta$ -MnO<sub>2</sub> (5.5) >  $\alpha$ -MnO<sub>2</sub> (4.1) >  $\gamma$ -MnO<sub>2</sub> (2.8) >  $\beta$ -MnO<sub>2</sub> (2.4). Generally, the oxidation reactions such as CO and NO oxidation on MnO<sub>x</sub> catalysts follow the Mars-van Krevelen mechanism,<sup>43, 44</sup> implying that lattice oxygen concentration could dominate the activity during the reaction.<sup>45</sup> Lee et al.<sup>44</sup> has observed that MnO<sub>2</sub> with more lattice oxygen was more active than Mn<sub>2</sub>O<sub>3</sub> for the oxidation of NO to NO<sub>2</sub>. Tang et al.<sup>26</sup> have observed that the richer lattice oxygen in Mn-Ce composite catalyst were advantage for the HCHO oxidation. In this study, the surface molar ratio of O<sub>latt</sub>/O<sub>ads</sub> exhibited the aligned orders to that of the catalytic activities for HCHO oxidation among the four types of MnO<sub>2</sub> catalysts, indicating that the activity is also closely related to the surface concentrations of O<sub>latt</sub> species. The abundant lattice oxygen, such as that on the  $\delta$ -MnO<sub>2</sub>, would lead to the excellent activity of MnO<sub>2</sub> catalysts for HCHO oxidation. However, this conclusion is just deduced from the XPS data, and to our knowledge, no previous report directly demonstrates the function of lattice oxygen in MnO<sub>2</sub> for HCHO catalytic oxidation. Furthermore, one recent study has claimed that the adsorbed oxygen species might play an important role in the total oxidation of toluene over MnO<sub>2</sub> catalysts.<sup>46</sup> Thus, the function of lattice oxygen needs to be verified by solid experimental data.

### 3.7 Lattice Oxygen Test

To confirm the role of lattice oxygen species on MnO<sub>2</sub> in this

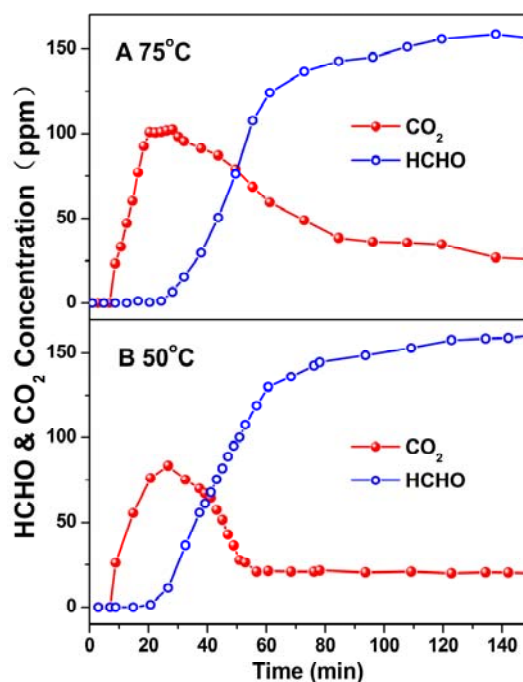


Fig. 8 Concentration variations of HCHO and CO<sub>2</sub> with the reaction time line in the lattice oxygen test.

reaction, the  $\delta$ -MnO<sub>2</sub> was next tested in the absence of oxygen in reaction gases. The details about the pretreatment of catalyst were given in experimental section. Fig. 8 shows the concentration of both HCHO and CO<sub>2</sub> as the function of time in the lattice oxygen test. After introducing HCHO into reactor, CO<sub>2</sub> concentration first



rapidly increased to a maximum and then descended gradually to a low level. HCHO was detected in outlet gas after about 20 min and then its concentration slowly increased to a high level. It is noted that CO<sub>2</sub> concentration generated in the 75 °C test was much higher than that in the 50 °C test, showing that the active oxygen species in δ-MnO<sub>2</sub> was much more active in 75 °C than 50 °C. The ratio of consumption oxygen to total oxygen in δ-MnO<sub>2</sub> catalyst was stoichiometrically calculated based on the amount of CO<sub>2</sub> production. It is shown that the 1.78% and 3.87% oxygen species were consumed during the 120 min reaction at 50 °C and 75 °C, respectively. After purged by pure N<sub>2</sub> for 30 min at 150 °C, there would be exclusive surface adsorbed oxygen and lattice oxygen species left on pretreated catalyst surface. However, as shown in Figure 6, no peak corresponding to surface adsorbed oxygen species was observed in H<sub>2</sub>-TPR profile, indicating that the amount of surface adsorbed oxygen species should be in considerably low level. As to the quantitative analysis, such a large amount of consumed oxygen during reaction should mostly come from the lattice oxygen. Therefore, the high HCHO conversion rates in both tests would be attributed to the activated abounding surface lattice oxygen. The results confirmed that the lattice oxygen species was responsible for the total oxidation of HCHO over MnO<sub>2</sub> catalysts.

Interestingly, the longer lasting production of CO<sub>2</sub> in 75 °C test, especially the gradually slowing down production rate from 60 minute to 100 minute indicates there might be the lattice oxygen mobility from the bulk to the surface. After the surface lattice oxygen being partly consumed, the subsurface oxygen even the more inner ones gradually shifted to the surface to participate the oxidation reaction. As the mobility became lower with its location from surface to inner, the supplement rate of oxygen species gradually slowed down, thus led to the drop of CO<sub>2</sub> production.

### 3.8 HCHO-TPD

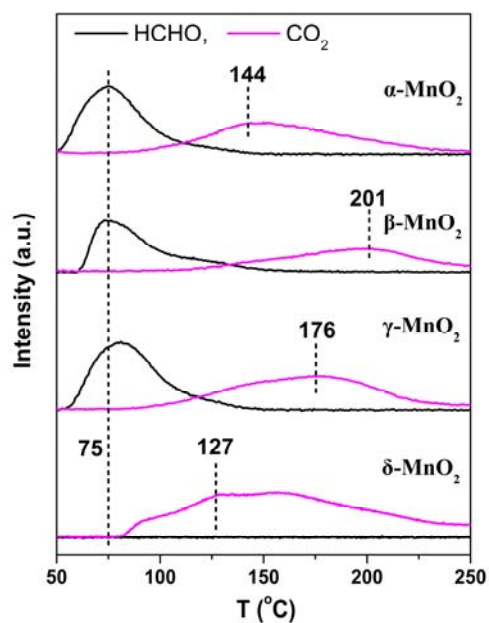


Fig. 9 HCHO-TPD results of  $\alpha$ -,  $\beta$ -,  $\gamma$ - and  $\delta$ -MnO<sub>2</sub> catalysts.

To investigate the adsorption/desorption properties of HCHO on the surfaces of the MnO<sub>2</sub> catalysts, HCHO-TPD were next carried out. As shown in Fig. 9, the HCHO were desorbed at around 50 °C and then reached the peaks at about 75 °C on the  $\alpha$ -,  $\beta$ -, and  $\gamma$ -MnO<sub>2</sub>

catalysts, while no HCHO desorption was observed on  $\delta$ -MnO<sub>2</sub>. The CO<sub>2</sub> were detected on all samples during the HCHO-TPD starting at around 75 °C with the peaks at 144 °C, 201 °C, 176 °C and 127 °C, respectively. The CO<sub>2</sub>-TPD have been also performed, and the results (supplementary information, Fig. S5) show that the CO<sub>2</sub> desorption temperatures on four catalysts were all lower than 100 °C, confirming that the CO<sub>2</sub> in the HCHO-TPD was mainly produced by the oxidation of some adsorbed HCHO or intermediates<sup>47</sup>. Therefore, HCHO desorption and CO<sub>2</sub> production should be closely dependent on the activity of surface lattice oxygen species. When the lattice oxygen species is highly active at low temperature, such as on  $\delta$ -MnO<sub>2</sub> catalyst, all adsorbed HCHO would be oxidized into CO<sub>2</sub> without desorption during the ramping temperature.

## 4. Conclusions

In summary, we prepared the  $\alpha$ -,  $\beta$ -,  $\gamma$ - and  $\delta$ - type of MnO<sub>2</sub> catalysts and observed their much different activities for the catalytic oxidation of HCHO. This enormous difference in activities is originated from their different physical properties on surface, K<sup>+</sup> volume, tunnel structures, the mobility of oxygen species, lattice oxygen abundances and also HCHO adsorption/desorption properties. However, the tunnel structures and lattice oxygen mobility and abundances might play more important role in HCHO oxidation reaction. The  $\delta$ -MnO<sub>2</sub> has a special 2D layer tunnel structure and also contains the most active oxygen species and the highest amount of lattice oxygen species on catalyst surface, therefore, presenting the highest activity in the four types of MnO<sub>2</sub> catalysts. Moreover, due to the high catalytic performance and facile preparation process, the  $\delta$ -MnO<sub>2</sub> may potentially be used as a support in applications of supported catalysts.

## Acknowledgements

This work was financially supported by the National Natural Science Foundation of China (21422706) and the Program of the Ministry of Science and Technology of China (2012AA062702).

## Notes and references

State Key Joint Laboratory of Environment Simulation and Pollution Control, Research Center for Eco-Environmental Sciences, Chinese Academy of Sciences, 18 Shuangqing Road, Beijing 100085, China. Fax: (+86) 10-62849121; Tel: (+86) 10-62849121; E-mail: cbzhang@cees.ac.cn

1. Y. Sekine, *Atmos. Environ.*, 2002, **36**, 5543.
2. J. Pei and J.Zhang, *Hvac&R Research*, 2011, **17**, 476.
3. R. Maddalena, M. Russell, D. Sullivan and M. Apte, *Environ. Sci. Technol.*, 2009, **43**, 5626.
4. J. Yang, Y. Qin, Y. Zeng and X. Ding, *Food Sci.*, 2014, **35**, 294.
5. J. Shie, C. Lee, C. Chiou, C. Chang, C. Chang and C. Chang, *J. Hazard. Mater.*, 2008, **155**, 164.
6. T. Noguchi and A. Fujishima, *Environ. Sci. Technol.*, 1998, **32**, 3831.
7. M. Chang and C. Lee, *Environ. Sci. Technol.*, 1995, **29**, 181.
8. C. Ma, X. Li and T. Zhu, *Carbon*, 2011, **49**, 2873.
9. C. Zhang, F. Liu, Y. Zhai, H. Ariga, N. Yi, Y. Liu, K. Asakura, M. Flytzani-Stephanopoulos and H. He, *Angew. Chem. Int. Ed.*, 2012, **51**, 9628.
10. B. Bai, H. Arandiyan and J. Li, *Appl. Catal., B*, 2013, **142**, 677.
11. C. Zhang, H. He and K. Tanaka, *Appl. Catal., B*, 2006, **65**, 37.



12. T. Quiroz, S. Royer, J. Bellat, J. Giraudon and J. Lamonier, *ChemSusChem*, 2013, **6**, 578.
13. C. Zhang and H. He, *Catal. Today*, 2007, **126**, 345.
14. B. Liu, Y. Liu, C. Li, W. Hu, P. Jing, Q. Wang and J. Zhang, *Appl. Catal., B*, 2012, **127**, 47.
15. B. Liu, C. Li, Y. Zhang, Y. Liu, W. Hu, Q. Wang, L. Han and J. Zhang, *Appl. Catal., B*, 2012, **111**, 467.
16. X. Tang, J. Chen, X. Huang, Y. Xu and W. Shen, *Appl. Catal., B*, 2008, **81**, 115.
17. H. Huang and D. Leung, *ACS Catal.*, 2011, **1**, 348.
18. C. Zhang, Y. Li, Y. Wang and H. He, *Environ. Sci. Technol.*, 2014, **48**, 5816.
19. C. Shi, B. Chen, X. Li, M. Crocker, Y. Wang and A. Zhu, *Chem. Eng. J.*, 2012, **200**, 729.
20. Z. Qu, S. Shen, D. Chen and Y. Wang, *J. Mol. Catal. A: Chem*, 2012, **356**, 171.
21. Z. Huang, X. Gu, Q. Cao, P. Hu, J. Hao, J. Li and X. Tang, *Angew. Chem. Int. Ed.*, 2012, **51**, 4198.
22. Q. Wang, W. Jia, B. Liu, W. Zhao, C. Li, J. Zhang and G. Xu, *Chem. Asian. J.*, 2012, **7**, 2258.
23. L. Zhou, J. He, J. Zhang, Z. He, Y. Hu, C. Zhang and H. He, *J. Phys. Chem. C*, 2011, **115**, 16873.
24. L. Ma, D. Wang, J. Li, B. Bai, L. Fu and Y. Li, *Appl. Catal., B*, 2014, **148**, 36.
25. L. Nie, J. Yu, X. Li, B. Cheng, G. Liu and M. Jaroniec, *Environ. Sci. Technol.*, 2013, **47**, 2777.
26. X. Tang, Y. Li, X. Huang, Y. Xu, H. Zhu, J. Wang and W. Shen, *Appl. Catal., B*, 2006, **62**, 265.
27. H. Chen, J. H., C. Zhang and H. He, *J. Phys. Chem. C*, 2007, **111**, 18033.
28. T. Chen, H. Dou, X. Li, X. Tang, J. Li and J. Hao, *Microporous Mesoporous Mater.*, 2009, **122**, 270.
29. Y. Wang, A. Zhu, B. Chen, M. Crocker and C. Shi, *Catal. Commun.*, 2013, **36**, 52.
30. S. Liang, F. Bulgan, R. Zong and Y. Zhu, *J. Phys. Chem. C*, 2008, **112**, 5307.
31. S. Turner and P. Buseck, *Science*, 1979, **203**, 456.
32. Y. Chabre and J. Pannetier, *Prog. Solid State Chem.*, 1995, **23**, 1.
33. J. Post and D. Veblen, *American Mineralogist*, 1990, **75**, 477.
34. J. Hou, L. Liu, Y. Li, M. Mao, H. Lv and X. Zhao, *Environ. Sci. Technol.*, 2013, **47**, 13730.
35. S. Devarajand N. Munichandraiah, *J. Phys. Chem. C*, 2008, **112**, 4406.
36. A. Wollner, F. Lang, H. Schmelz and H. Knozinger, *Appl. Catal., A*, 1993, **94**, 181.
37. M. Toupin, T. Brousse and D. Belanger, *Chem. Mater.*, 2004, **16**, 3184.
38. S. Cai, D. Zhang, L. Zhang, L. Huang, H. Li, R. Gao, L. Shi and J. Zhang, *Catal. Sci. Technol.*, 2014, **4**, 93.
39. B. Tan, K. Klabunde and P. Sherwood, *J. Am. Chem. Soc.*, 1991, **113**, 855.
40. X. Tang, J. Chen, Y. Li, Y. Li, Y. Xu and W. Shen, *Chem. Eng. J.*, 2006, **118**, 119.
41. C. Yu, G. Li, L. Wei, Q. Fan, Q. Shu and J. Yu, *Catal. Today*, 2014, **224**, 154.
42. J. Li, C. Song and S. Liu, *Acta Chimica Sinica*, 2012, **70**, 2347.
43. R. Xu, X. Wang, D. Wang, K. Zhou and Y. Li, *J. Catal.*, 2006, **237**, 426.
44. S. Lee, K. Park, S. Kim, D. Kwon and S. Hong, *J. Air Waste Manage. Assoc.*, 2012, **62**, 1085.
45. W. Song and E. Hensen, *Catal. Sci. Technol.*, 2013, **3**, 3020.
46. F. Wang, H. Dai, J. Deng, G. Bai, K. Ji and Y. Liu, *Environ. Sci. Technol.*, 2012, **46**, 4034.
47. G. Busca, J. Lamotte, J. Lavalley and V. Lorenzelli, *J. Am. Chem. Soc.*, 1987, **109**, 5197.